Aerospace Science and Technology 73 (2018) 332–342

Contents lists available at ScienceDirect

Aerospace Science and Technology

www.elsevier.com/locate/aescte

# Numerical investigation of the axial impulse load during the startup in the shock tunnel

Baoqing Meng [a,b], Guilai Han [a,b,*], Changtong Luo [a,b], Zonglin Jiang [a,b]

[a] State Key Laboratory of High-temperature Gas Dynamics, Institute of Mechanics, Chinese Academy of Sciences, 100190 Beijing, China
[b] University of Chinese Academy of Sciences, 100049 Beijing, China

ARTICLE INFO

*Article history:*
Received 15 May 2017
Received in revised form 1 December 2017
Accepted 7 December 2017
Available online 13 December 2017

*Keywords:*
Hypersonic
Shock tunnel
Start-up process
Impulse force
Vibration

ABSTRACT

A shock tunnel is a representative type of ground-based equipment in the hypersonic field, which has the advantage of free stream of excellent quality. Accurate measurements of aerodynamic forces in the shock tunnel are great challenges. The impulse loads during the start-up process induce the vibration of the model and its support. Aerodynamic signals are disturbed by vibrational signals. The identification of the starting time of the steady periodic vibration and excited natural frequencies of the whole structure would contribute to improve the accuracy of measurement. These two factors are closely related to the properties of the impulse forces. However, there is currently no published research on the impulse forces. In this paper, the type of impulse forces (drag history) acting on the sharp cone during the start-up process was investigated by numerical simulation. The distribution of the static pressure of the typical wave structures was found to have a significant influence on the types of the drag history. A formula, based on the physical analysis of start-up process, was put forward to estimate the starting time of the steady stage. Additionally, the subsequent analysis and design optimization such as vibration of structure and disturbing frequencies needed an analytical and simple formation of drag history. Thus, the drag history was approximated by numbers of sine functions. Different phases exhibited notable difference in composition. Also, a metric denoted as the energy coefficient was derived to identify the critical frequencies and simplify the analytical expression of the impulse force.



## 1. Introduction

A shock tunnel is a representative type of ground-based equipment in the hypersonic field, which has the advantages of high total pressure, high total temperature and low cost. As a typical piece of impulse equipment, the operational time of a shock tunnel is extremely short, with a test time that is usually in the range of 2–30 ms [1,2]. Such a short running time constitutes a great challenge regarding the accurate measurement of the aerodynamic force. For a conventional tunnel, the running time is generally several minutes, i.e., a much longer time than the vibration period of the force measurement structure, which includes a sting support, measurement components and the aircraft model. The effects of damping are obvious, and the whole structure can reach a force equilibrium condition. The measurement is quasi-static, and the high accuracy of the measurement can be ensured, but, there are essential differences for the force measurements in the shock tunnel. Nevertheless, the effects of vibration damping can be neglected because the order of magnitude of the test time is the same as that of the period of the force measurement structure. Therefore, the measurement of the balance of aerodynamic forces is a dynamic process. In addition, only several periods of signals can be obtained from the outputs of the balance. Also, due to the essentially different mechanical state of the force measurement systems during testing, the difficulty and accuracy of the force measurement in the shock tunnel are evidently different from those in a conventional tunnel.

The vibration of the force measurement structure in the shock tunnel is initiated by the impulse aerodynamic force during the nozzle start-up process, and the whole structure reaches a steady periodic vibration around the equilibrium position during the test period. The signals sensed by the balance are a combination of the aerodynamic force signals and vibrational signals. The removal of the vibrational signals is essential for force signal processing in the shock tunnel. Several methods have been developed for the peeling of the signals, including one technique that is commonly used, namely the acceleration compensation force balance technique [3–7]. The accelerometers are mounted near the measurement component and the acceleration signals are measured

* Corresponding author at: State Key Laboratory of High-temperature Gas Dynamics, Institute of Mechanics, Chinese Academy of Sciences, 100190 Beijing, China.
*E-mail address:* hanguilai@imech.ac.cn (G. Han).

https://doi.org/10.1016/j.ast.2017.12.013
1270-9638/

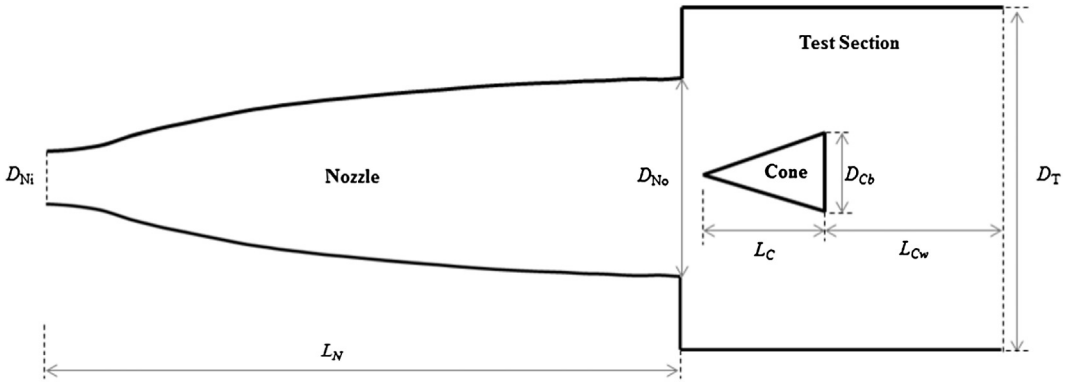


**Fig. 1.** Schematic drawing of the computational domain.

along with the force signals. The plat force signals are obtained by adding the processed acceleration signals to the force signals. The acceleration signals supplied by accelerators can only display the frequencies of free vibration properties at a certain position with very limited information on the vibration. Another method involves using the average to counteract the fluctuation of the selected signals. For both of these methods, the detailed understanding of the starting time of the steady periodic duration and disturbing frequencies are very important to ensure the accuracy of the force measurements. The start-up stage and the following steady vibration comprise the whole process of the tunnel test. The starting time point is just the end of the start-up stage. Accordingly, the time of duration of the impulse force should be identified. Also, the vibrational theory indicates that the initial condition of the steady vibration depends on the start-up stage. Thus, the form and frequency composition of the impulse force need to be investigated. However, no research on the characteristics of the impulse forces during start-up of shock tunnel has been reported to date.

Meanwhile, the wave structures of the nozzle start-up process have been investigated in numerous studies involving a shock tunnel [8–14]. Typical wave structures consisting of primary shock (PS), secondary shock (SS) and contact discontinuity (CD) have been observed during the start-up process of the nozzle of the shock tunnel. The typical wave structures indicate that the pressure distribution around the center zone of the nozzle has a certain commonality for different nozzles in a shock tunnel. Thus, common characteristics exist for the impulse drag-time curve acting on an aircraft model.

This paper described the study of the various characteristics of an axial impulse force history acting on a sharp cone during the start-up process of the JF12 shock tunnel. The JF12 hypersonic shock tunnel was successfully developed by Jiang et al. [15] at the Institute of Mechanics Chinese Academy of Sciences (CAS). The wave structures and mechanisms of the impulse force were also investigated. A formula based on the physical analysis of the start-up process, was put forward to estimate the starting time of the steady stage. Furthermore, the subsequent analysis and design optimization such as vibration of structure and disturbing frequencies needed an analytical and simple formation of drag history. Additionally, analytical modeling with numbers of sine functions for the impulse force was conducted, this approach made the theoretical study of the subsequent analysis of the vibrational properties possible. Further studies aimed at simplifying the analytical form of impulse force were also conducted. The simplification should be based on a metric to identify the critical frequencies. A metric denoted as the energy coefficient was derived based on the vibrational theory. The number of the sine functions was replaced by only three significant sine functions and an acceptable substitution effect was obtained.

**Table 1**
Dimension of the computational domain.

| Definition | Dimension (mm) |
|---|---|
| $D_{Ni}$ | 310.0 |
| $D_{No}$ | 2457.8 |
| $L_N$ | 14250.0 |
| $D_{Cb}$ | 529.0 |
| $L_C$ | 1500.0 |
| $D_T$ | 3500.0 |

## 2. Numerical method

### 2.1. Computational domain and grid generation

The computational domain contains a nozzle of 14.2 m in length and 2.5 m in diameter, a test section and a sharp cone with a semi angle of 10°, as shown in Fig. 1. **The calibrated results of the flow showed that the deviation of the Mach number around the effective region of the nozzle outlet was less than 2%.** The flow was simplified to be axisymmetric and the computational domain was simplified to a two-dimensional region. Only the properties of the axis forces were of interest in the current study and the effects of the flow asymmetry were beyond the scope of this research. The detailed dimensions of each section are listed in Table 1. $L_N$, $L_C$ and $L_{cw}$ denote the length of the nozzle, sharp-cone, and wake region, respectively; $D_{Ni}$, $D_{No}$, $D_{Cb}$ and $D_T$ represent the diameters of the nozzle throat, nozzle outlet, cone base and test section, respectively.

The whole domain was divided into six blocks for grid generation and computational purposes, as shown in Fig. 2. Because the finite difference method and structural meshes were used, mesh orthogonality was important to achieve an accurate calculation. An orthogonal mesh approach proposed by Volkan Akcelik [16] was used for grid generation; this method ensured the mesh orthogonality in the inner flow field. In addition, the mesh orthogonality near the wall was also ensured by creating vertical lines to the boundary lines passing through the inner gird points. A total of five separate grids were used for grid independence verification. Each grid described in Table 2 was obtained from the previous grid by doubling the number of grids in the $i$ and $j$ directions.

### 2.2. Governing equation and algorithm

The two-dimensional axisymmetric and compressible Navier–Stokes equations with transformation to the computational space [17] presented in eq. (1) were used for the calculation. The convective term was solved using the NND scheme [18], and the viscous term was discretized using the second-order central difference method. The first-order Runge–Kutta method was applied

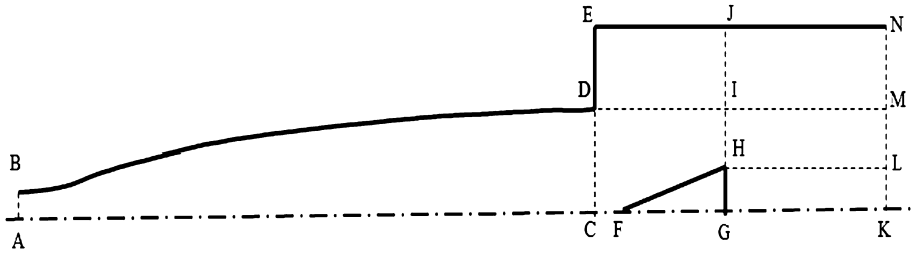


**Fig. 2.** Schematic of the block division for grid generation and computation.

**Table 2**
Five different resolutions for each grid system.

| | Case I | Case II | Case III | Case IV | Case V |
|---|---|---|---|---|---|
| Grid points | 97,213 | 354,626 | 1,412,386 | 5,640,021 | 21,883,041 |

**Table 3**
Initial parameters of the flow field.

| Parameters | Nozzle state | Vacuum state |
|---|---|---|
| $P$ (Pa) | $1.16 \times 10^6$ | 50.0 |
| $T$ (K) | 1833.3 | 300.0 |
| $u$ (m/s) | 858.3 | 0.0 |
| $v$ (m/s) | 0.0 | 0.0 |

for time integration. The message passing interface (MPI) parallel programs were applied in the program. In addition, the axis of the nozzle was defined as the $x$-axis and was set as an axisymmetric boundary based on a previously reported method given [17]. The parameters of the nozzle inlet for the initial state are denoted as nozzle state, as shown in Table 3, and the parameters of the other regions are denoted as vacuum state. The total pressure was $p_0 = 2.2$ MPa, and the total temperature was $T_0 = 2200$ K.

$$\frac{\partial \overline{Q}}{\partial \tau} + \frac{\partial \overline{E}}{\partial \xi} + \frac{\partial \overline{F}}{\partial \eta} + \bar{H} = \frac{\partial \overline{E}_v}{\partial \xi} + \frac{\partial \overline{F}_v}{\partial \eta} + \overline{H}_v \tag{1}$$

$$\overline{Q} = \frac{Q}{J} \tag{1a}$$

$$\overline{E} = \frac{1}{J}[\xi_t Q + \xi_x E + \xi_y F] \tag{1b}$$

$$\overline{E} = \frac{1}{J}[\xi_t Q + \xi_x E + \xi_y F] \tag{1c}$$

$$\overline{F} = \frac{1}{J}[\eta_t Q + \eta_x E + \eta_y F] \tag{1d}$$

$$\overline{H} = \frac{1}{J} H \tag{1e}$$

$$\overline{E}_v = \frac{1}{J}[\xi_x E_v + \xi_y F_v] \tag{1f}$$

$$\overline{F}_v = \frac{1}{J}[\eta_x E_v + \eta_y F_v] \tag{1g}$$

$$\overline{H}_v = \frac{1}{J} H_v \tag{1h}$$

$$Q = \begin{bmatrix} \rho \\ \rho u \\ \rho v \\ \rho e_t \end{bmatrix} \tag{1i}$$

$$E = \begin{bmatrix} \rho u \\ \rho u^2 \\ \rho u v \\ (\rho e_t + p) u \end{bmatrix} \tag{1j}$$

$$F = \begin{bmatrix} \rho v \\ \rho u v \\ \rho v^2 + p \\ (\rho e_t + p) v \end{bmatrix} \tag{1k}$$

$$H = \begin{bmatrix} \rho v \\ \rho u v \\ \rho v^2 \\ (E + p) v \end{bmatrix} \tag{1l}$$

$$E_v = \begin{bmatrix} 0 \\ \tau_{xxp} \\ \tau_{xy} \\ u\tau_{xxp} + v\tau_{xy} - q_x \end{bmatrix} \tag{1m}$$

$$F_v = \begin{bmatrix} 0 \\ \tau_{xy} \\ \tau_{yyp} \\ u\tau_{xy} + v\tau_{yyp} - q_y \end{bmatrix} \tag{1n}$$

$$H_v = \begin{bmatrix} 0 \\ \tau_{xy} - \frac{2}{3} y \frac{\partial}{\partial x}(\frac{\mu v}{y}) \\ \tau_{yy} - \tau_{\theta\theta} - \frac{2}{3}\frac{\mu v}{y} - \frac{2}{3} y \frac{\partial}{\partial y}(\frac{\mu v}{y}) \\ u\tau_{xy} + v\tau_{yy} - \frac{2}{3}\frac{\mu v^2}{y} - \frac{2}{3} y \frac{\partial}{\partial y}(\frac{\mu v^2}{y}) - \frac{2}{3} y \frac{\partial}{\partial x}(\frac{\mu u v}{y}) - q_y \end{bmatrix} \tag{1o}$$

The equation of the state is given in eq. (2).

$$P = \rho R T \tag{2}$$

### 2.3. The validation of the code

The code was validated by numerous cases and three classical cases were computed by the computational fluid dynamics (CFD) code used in this study. The computed results were compared with experimental results. Good agreements were observed between computed and experimental results, as shown in Fig. 3(a–d). Additionally, the measured drag coefficients of the spheres are also shown in Fig. 3(e). Specifically, for $M_\infty > 4$, the measured drag coefficients lay between 0.87 and 0.90 and the numerical results lay between 0.8713 and 0.8910, which validated the reliability of the aerodynamic computation of the code used.

### 2.4. Grid independence verification

The simulation results were sensitive to the number of resolutions. A plot of the Mach number distribution of the nozzle outlet at the steady-state condition is shown in Fig. 4 for five different meshes. Data for all the Mach numbers were extracted from the same position. The results of cases I and II did not capture both the height and the shape of the Mach number distribution. Thus, it was impossible to distinguish the detailed flow structure with

(a) (b)[19]

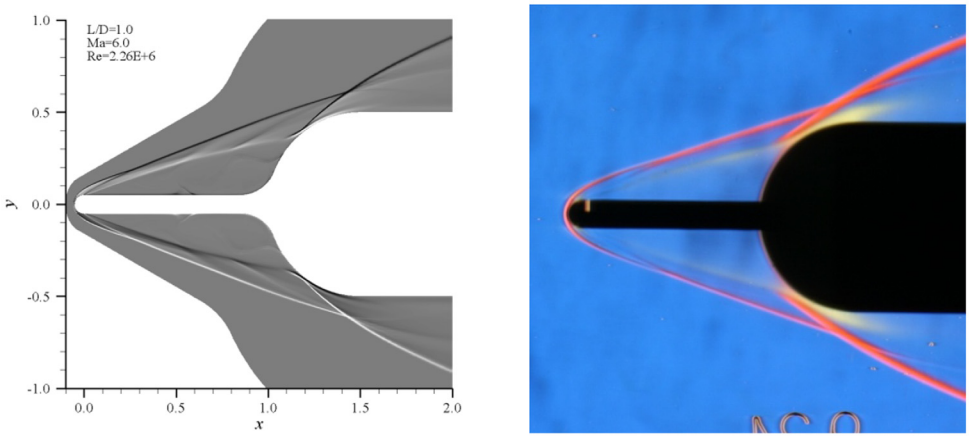


(c) (d)[20]

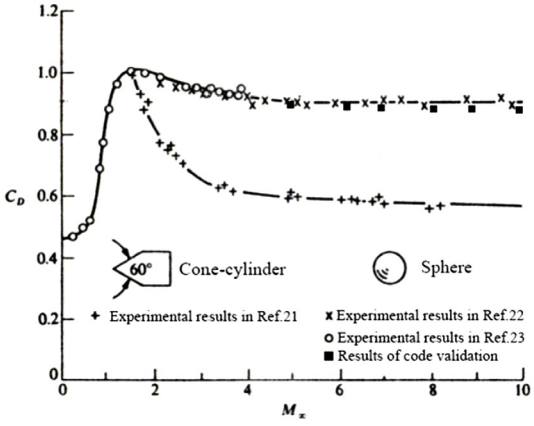


(e)[21-24]

**Fig. 3.** Validation of the code used. An unsteady flow of shock wave diffraction over a rectangular block: (a) Numerical results, (b) Experimental results. Hypersonic flow over a spiked-nose blunt body configuration: (c) Numerical results, (d) Experimental results, (e) Plots of the drag coefficients of experimental and numerical results at different Mach number.

these coarse grids. The values of case III were close to the results of cases IV and V, except for the positions of the boundary layer. In addition, the values and shapes of cases IV and V were very close, and the numerical results were in good agreement with the experimental results. The experimental data were derived from the experimental calibration of the flow field in the JF12 shock tunnel. In other words, more refinement of the resolution would not significantly change the flow results. Accordingly, the resolution of case IV was chosen for the ensuring simulations to generate the results.

## 3. Characteristics of the drag-time curve

### 3.1. Evolution of the wave structures during the start-up process

The evolution of the wave structure of the whole process is displayed in Fig. 5(a–k). At the beginning of the start-up process, the propagation of the PS was clearly observed. A CD following the PS was identified by comparing the density and pressure fields. In addition, the contact discontinuity became unstable and twisted. A lambda-shaped shock appeared because of the interaction of the

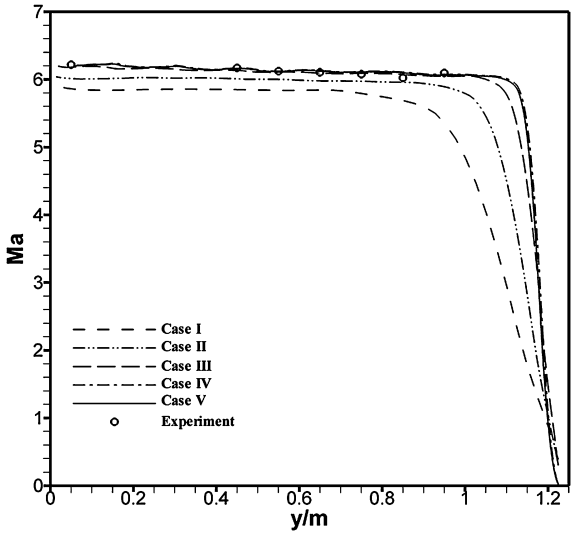


**Fig. 4.** Mach number distribution of the nozzle outlet for different cases.

boundary layer and PS near the wall area. In addition, this configuration shock propagated downstream with the PS. The SS appeared and propagated at a very high Mach number (approximately 13 in this case) to match the low pressure downstream of the throat and the high pressure behind the CD. Near the outlet of the nozzle, the wave structures that contain PS, CD and SS remain in a similar configuration because the section area of the nozzle is essentially constant. The wave structures flowed into the test section and acted on the sharp cone. When the steady air following the wave structures acted on the sharp cone, a steady flow field was generated.

### 3.2. Dynamic course and characteristics of force

The total drag ($F_{DT}$), is a combination of the forebody pressure drag ($F_{Dp}$), base drag ($F_{Db}$) and forebody friction drag ($F_{Df}$). In this study, the $F_{Dp}$ was prominent in the composition of the $F_{DT}$ during the whole process, as shown in Fig. 6. The drag-time curve of the $F_{DT}$ could be divided into the unsteady (AF) stage and the steady stage, which has a constant value. The AF stage comprised stage AE (defined as the impulse stage) and stage EF (defined as the transition stage). During stage AE, the time-force curve varied significantly in an extremely short time, on the order of milliseconds, and presented typical features of the impulse force during the start-up process of the nozzle. In addition, the vibration of the force measurement structure was triggered by rapid and considerable variation. Thus, stage AE was defined as the impulse stage. During stage EF, the curve displayed an entirely different shape. There was a relatively slow rise until the total force and flow field achieved stability. Stage EF played a role in the transition between the impulse stage AE and the steady stage.

Further analysis showed that the trend of the drag-time curve was closely related to the wave structure and static pressure distribution of the wave structure when the PS arrived at the outlet of the nozzle, as shown in Fig. 5(e). The pressure distribution along the axis of the nozzle displayed two high-pressure regions (denoted as I and III in Fig. 5(f)) that were followed by low-pressure regions (denoted as II and IV, in Fig. 5(f)). Additionally, the average pressure value and the space span of region III were larger than those of region I.

Both the drag-time curve and the pressure distribution (illustrated in Fig. 5(f)) exhibited a double-peak shape, and detailed examinations regarding the correspondence between them both were conducted. The drag-time curve started to rise at point A, as indicated in Fig. 6, at which time the PS reached the tip of the cone corresponding to Fig. 5(f). The air from the high-pressure region I flowed over the forebody of the cone in Fig. 5(g); this period corresponded to stage AB with uptrend. The low-pressure region II behind region I flowed over the cone resulting in the reducing trend of curve BC. The drag-time curve reached the first peak at point B, whose flow field is shown in Fig. 5(h), and the first valley at point C is shown in Fig. 5(i). The trend of curve AC depended on the combined effects of the high-pressure region I and low-pressure region II. The high and low distributions of the pressure caused the increases and decreases of the drag. The similar trends of stage CD and stage DE were determined by region III and region IV. The values of the second peak and valley appeared at point D and point E, whose wave structures are shown in Fig. 5(j) and Fig. 5(k), respectively. The larger length scale and pressure amplitude value of region III and region IV, shown in Fig. 5(e), caused larger fluctuation of curve CE. The curve reached the highest peak at point D and the lowest valley at point E.

### 3.3. Comparison of the numerical results with the experimental results

The drag coefficients $C_D$ and forebody drag coefficient $C_{DF}$ of the numerical result were compared with the experimental results when the flow field became steady, as shown in Table 4. Excellent agreements were observed between the numerical and experimental results. The differences mainly arose from the differences in the Reynolds number and the disturbances of the flow field induced by sting support in the experiments.

Additionally, the values of the $p_b/p_\infty$ (ratio of base pressure and pressure of the freestream) were compared with the experimental results, as shown in Table 5. The experimental data originated from the JF12 shock tunnel and the NAVSHIPRANDCEN hypersonic tunnel. The numerical result showed good agreement with the experimental results.

### 3.4. Characteristics of the time span for the drag-time curve

The whole drag-time curve describes the process of wave structures flowing over the cone. Accordingly, the time span of the impulse force was determined by the average velocity of the wave structure, the length scale of the wave structure and the aircraft model. The length scale of the aircraft model was known. Meanwhile, the average velocity of the wave structure could be estimated as the velocity of air at the outlet of the nozzle in steady flow. Also, the scale of the wave structure could be estimated by comparing the steady flow field with the wave structures at the time of the arrival of the PS at the nozzle outlet. In this case, the length scale was approximately 10 m for the nozzle, as shown in Fig. 7. In addition, the time span of the unsteady stage during the start-up process could be estimated as $t_i \approx 5.8$ ms, using eq. (3). The numerical results in Fig. 6 show that $t_{iCFD} \approx 6.0$ ms. The formation of the flow field around the cone base may make it longer than the estimated value.

$$t_i \approx \frac{L_C + L_w}{u_{out}} \tag{3}$$

### 3.5. Induced frequency distribution of the unsteady stage

The vibration of the force measurement structure resulted from a combination of each vibration mode with harmonic form. In addition, the modes were induced to different degrees, depending on the energy distribution of the induced force. The drag-time curve was divided into two stages, depending on different features. The data of the two stages were modeled by a nonlinear approximation to decompose the signals with a number of sine functions,

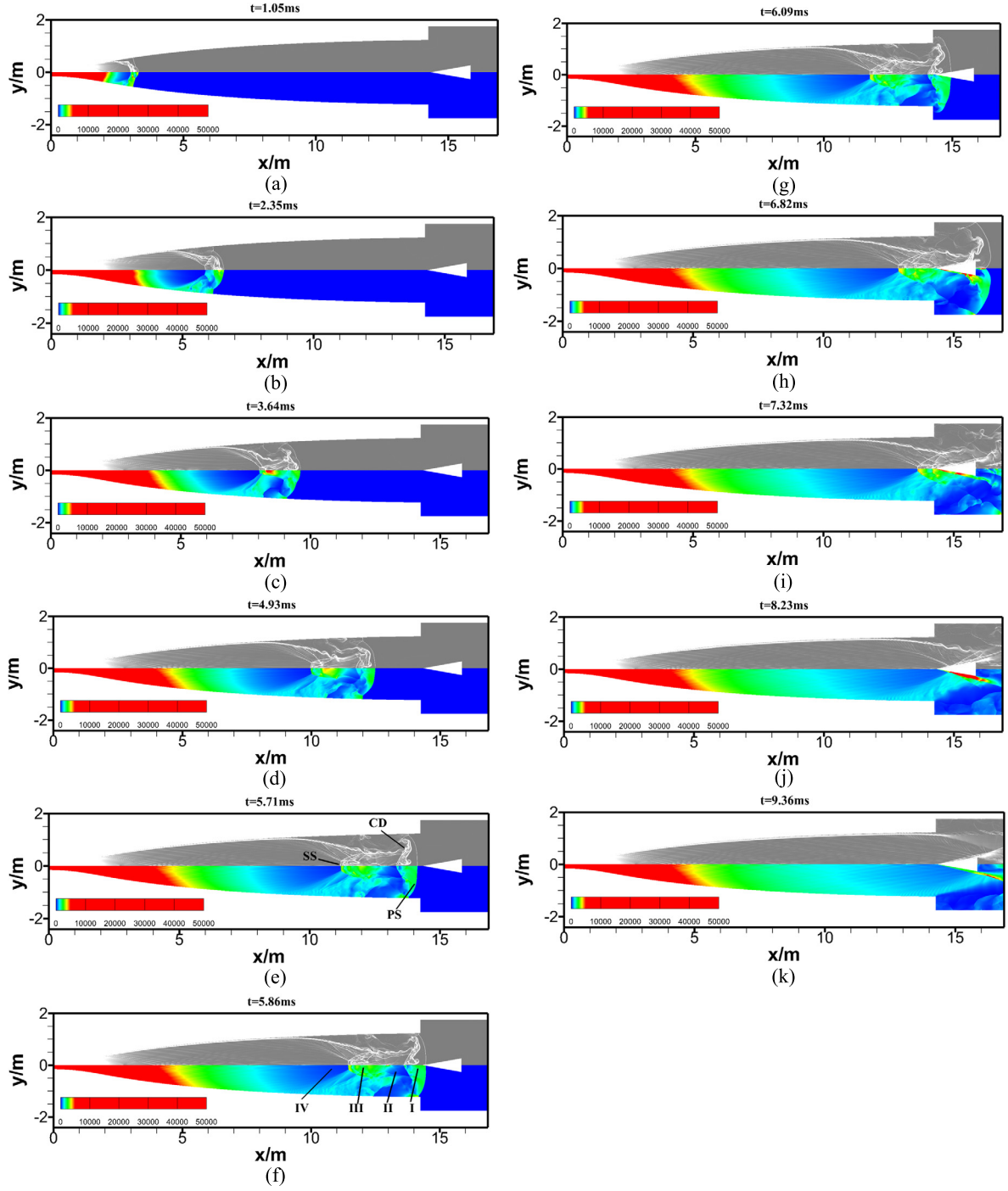


**Fig. 5.** Evolution of the process at different time visualized by the density gradient (upper) and the pressure (lower).

**Table 4**
Experimental and numerical results $C_D$ and $C_{DF}$ of the cone in hypersonic flow.

| | Ma | Re | $C_D$ | $C_{DF}$ |
|---|---|---|---|---|
| JF12 shock tunnel [19] | 6.15 | $1.38 \times 10^6$/m | 0.106 | 0.118 |
| CFD | 6.13 | $1.86 \times 10^6$/m | 0.097 | 0.111 |
| FD-07 tunnel [20] | 5.95 | $3.6 \times 10^7$/m | 0.120 | – |
| JF-4B [21] | 7.8 | $1.3.5 \times 10^7$/m | 0.123 | – |

**Table 5**
Values of the $p_b/p_\infty$ of a sharp cone with a semi angle of 10° in hypersonic flow.

| | Ma | Re | $p_b/p_\infty$ |
|---|---|---|---|
| JF12 shock tunnel [19] | 6.15 | $1.38 \times 10^6$/m | 0.47 |
| CFD | 6.13 | $1.86 \times 10^6$/m | 0.43 |
| NAVSHIPRANDCEN hypersonic tunnel [22] | 6.34 | $1.97 \times 10^6$/m | 0.4 |
| NAVSHIPRANDCEN hypersonic tunnel [22] | 6.34 | $0.98 \times 10^6$/m | 0.5 |

as shown in eq. (4). A global optimization algorithm, the Low Dimension Simplex Evolution (LDSE) [23], was applied to find the coefficients in the deposition model. The parameters of LDSE were set according to a previous report [24]. The approximation coefficients are listed in Table 6 and Table 7 in descending order of the absolute value of $a_k$. For stage AE, one of the prominent frequencies was 175.7 Hz, which was close to the prominent frequency of 178.1 Hz in stage EF. In addition, another two prominent fre-

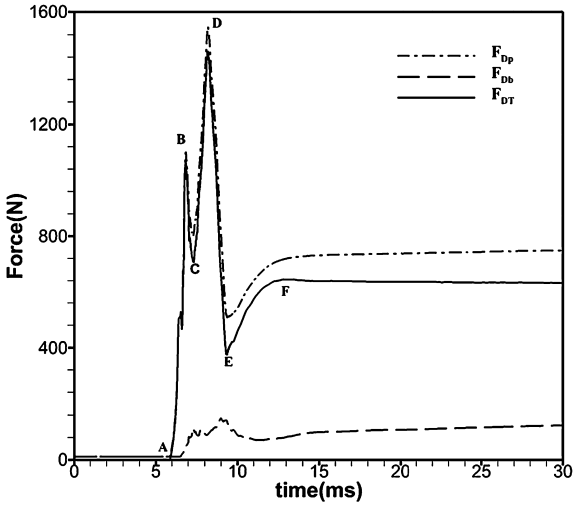


**Fig. 6.** Drag-time curve for the aerodynamic force from the start-up to the steady condition.

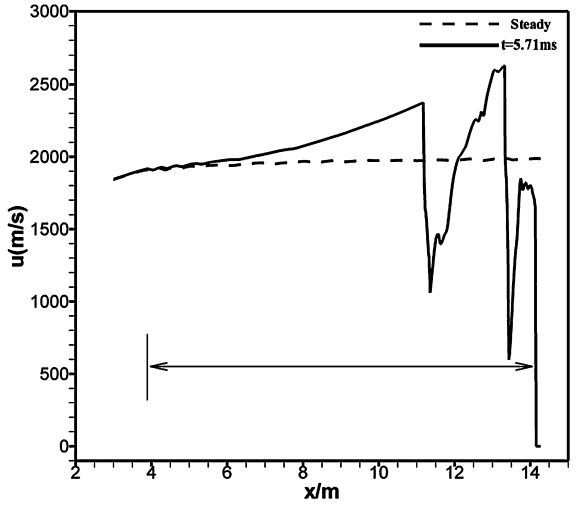


**Fig. 7.** Velocity distribution along the axis of the nozzle at the time of 5.71 ms and under steady condition.

**Table 6**
Approximation coefficients of stage AE, $N_k = 10$.

| | $f_k$ (Hz) | $a_k$ | $\Omega_k$ | $\phi_k$ |
|---|---|---|---|---|
| $k=1$ | 80.2 | 812.5 | 504.1 | 33.7 |
| $k=2$ | 175.7 | 2390.7 | 1104.1 | −13.3 |
| $k=3$ | 229.4 | 1249.9 | 1441.6 | 14.7 |
| $k=4$ | 729.3 | −205 | 4582.3 | −75.3 |
| $k=5$ | 1072.5 | 32.4 | 6738.8 | 114.3 |
| $k=6$ | 1670.8 | −1369.8 | 10498.1 | −20.2 |
| $k=7$ | 1677 | 1330.5 | 10536.8 | −20.3 |
| $k=8$ | 2356.2 | −69.4 | 14804.4 | 13.7 |
| $k=9$ | 2485.2 | −59.4 | 15615.1 | −22.8 |
| $k=10$ | 38599.7 | −0.2 | 242529 | −1526.6 |

quencies in stage AE were close to 1670 Hz, which is a much higher frequency. The characteristics of the two stages were significantly different. During the impulse stage AE, the drag-time curve showed a high frequency oscillation combined with a frequency of 175.7 Hz oscillation. For stage EF, there was only one prominent frequency, specifically at 178.1 Hz.

$$y = \sum_{k=1}^{N_k} a_k \sin(\Omega_k t + \phi_k) \tag{4}$$

**Table 7**
Approximation coefficients of stage EF, $N_k = 8$.

| | $f_k$ (Hz) | $a_k$ | $\Omega_k$ | $\phi_k$ |
|---|---|---|---|---|
| $k=1$ | 178.1 | 895.6 | 1119 | 2.3 |
| $k=2$ | 311.8 | 368.2 | 1959 | 1.5 |
| $k=3$ | 714.8 | 27.5 | 4491 | 5.1 |
| $k=4$ | 1358.4 | 7.3 | 8535 | 0.9 |
| $k=5$ | 1664.7 | 6.5 | 10460 | 1.2 |
| $k=6$ | 2040.4 | 2.854 | 12820 | 5 |
| $k=7$ | 2651.5 | 0.5993 | 16660 | −4.1 |
| $k=8$ | 3119.4 | 0.5003 | 19600 | −2.6 |

**Table 8**
Approximation coefficients of stage AF, $N_k = 12$.

| | $f_k$ (Hz) | $a_k$ | $\Omega_k$ | $\phi_k$ |
|---|---|---|---|---|
| $k=1$ | 77.6 | −1024.3 | 487.6 | −2.9 |
| $k=2$ | 166.6 | 197.7 | 1046.7 | 13.8 |
| $k=3$ | 315.6 | −325.3 | 1983.2 | 0.1 |
| $k=4$ | 651.9 | 334.1 | 4096 | 3.1 |
| $k=5$ | 705.3 | −237.8 | 4431.6 | 1.7 |
| $k=6$ | 1022.1 | 21.1 | 6421.9 | 0.8 |
| $k=7$ | 1518.2 | −57.8 | 9539.4 | −0.4 |
| $k=8$ | 1626.2 | −115 | 10217.8 | 6.3 |
| $k=9$ | 1676.1 | −69.1 | 10531 | 2 |
| $k=10$ | 2344.1 | −119.6 | 14728.5 | −0.01 |
| $k=11$ | 2405.7 | −392 | 15115.3 | 1.7 |
| $k=12$ | 2427.9 | −289.8 | 15255.1 | 10.6 |

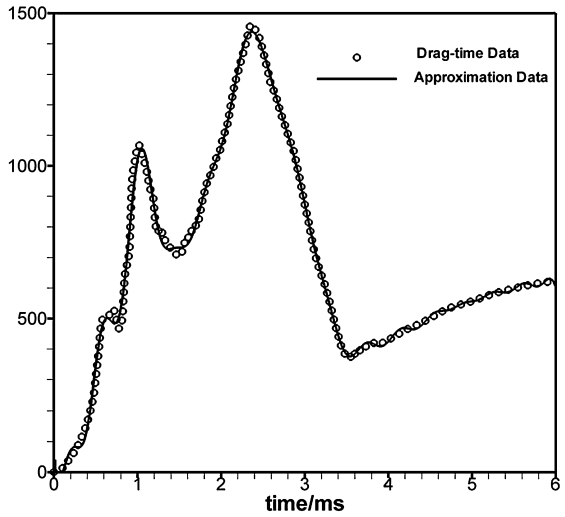


**Fig. 8.** Drag-time data and approximation data for the unsteady stage during the start-up process.

## 4. Modeling of the drag-time curve

### 4.1. Approximation of the unsteady stage of the drag-time curve

Theoretical analysis of the forced vibration requires an explicit function expression of the drag-time curve. The approximation for the whole unsteady stage AF was conducted for subsequent theoretical analysis with the form given by eq. (4), and the coefficients are listed in Table 8. The approximation results showed good agreement with the original drag-time curve data, except for minor differences around the peaks shown in Fig. 8. The approximation solution contained the primary features of the drag-time curve. The prominent frequency was approximately 77.6 Hz, which is close to the frequency of the first mode shape. The value of the second and third frequencies was greater than 2000 Hz and displayed the extremely short and impulsive characteristics of the drag-time curve during the start-up process.

### 4.2. Theoretical solutions of forced vibration

The drag-time curve during the start-up process was approximated by 12 sine-wave functions with 36 coefficients. Numerous undetermined coefficients were used to ensure the goodness of the approximation. Tail-supporting structures were applied for measurement of the force of the sharp cone model in the JF12 hypersonic shock tunnel. The basic configuration of the tail support was a cantilever beam [25]. A homogeneous material and constant-section beam model was used for theoretical analysis. The measurement cell of the balance was simplified to a certain section of the beam. The displacement and internal axis force proportional to the axis strain were the physical quantities measured in most experiments. Thus, these quantities were selected as the evaluation criterion for simplification of the approximated coefficients.

The oscillation equation [26] of the forced vibration for the constant-section beam model along the longitudinal direction is expressed by eq. (5):

$$\rho A\frac{\partial^2 u}{\partial t^2} = EA\frac{\partial^2 u}{\partial x^2} + P(x,t) \tag{5}$$

The outer induced drag-time curve encompasses the impulse force followed by a constant aerodynamic force $P_0$. The location of the acting force is denoted by the symbol $\xi$.

$$P(x,t) = \begin{cases} \sum_{k=1}^{12} a_k \sin(\Omega_k t + \phi_k)\delta(x-\xi), & 0 \le t \le t_F \\ P_0\delta(x-\xi), & t > t_F \end{cases} \tag{6}$$

The normal modes [26]:

$$U_i(x) = \sqrt{\frac{2}{\rho Al}}\sin\frac{(2i-1)\pi x}{2l} \quad i = 1,2,3\ldots \tag{7}$$

The natural frequencies [26]:

$$\omega_i = \frac{(2i-1)\pi}{2l}\sqrt{\frac{E}{\rho}} \quad i = 1,2,3\ldots \tag{8}$$

The generalized force:

$$q_{i(t)} = \int_0^l P_{(x,t)}U_{i(x)}\mathrm{d}x = \begin{cases} \sum_{k=1}^{12} a_k\sqrt{\frac{2}{\rho Al}}\sin[\frac{(2i-1)\pi\xi}{2l}]\sin(\Omega_k t+\phi_k), & 0 \le t \le t_F \\ P_0\sqrt{\frac{2}{\rho Al}}\sin[\frac{(2i-1)\pi\xi}{2l}], & t > t_F \end{cases} \tag{9}$$

The normal coordinate:

$$\eta_i(t) = \frac{1}{\omega_i}\int_0^t q_{i(\tau)}\sin\big[\omega_i(t-\tau)\big]\mathrm{d}\tau = \begin{cases} \sum_{k=1}^{12}\frac{-a_k}{2\omega_i}\sqrt{\frac{2}{\rho Al}}\sin(\frac{(2i-1)\pi\xi}{2l})\{\frac{[\sin(\Omega_k t+\phi_k)-\sin(\omega_i t+\phi_k)]}{\Omega_k-\omega_i} \\ \quad -\frac{[\sin(\Omega_k t+\phi_k)+\sin(\omega_i t-\phi_k)]}{\Omega_k+\omega_i}\}, \quad 0 \le t \le t_F \\ \eta_i(t_F)\cos[\omega_i(t-t_F)] + \frac{\dot\eta_i(t_F)}{\omega_i}\sin[\omega_i(t-t_F)] \\ \quad +\frac{P_0}{\omega_i^2}\sqrt{\frac{2}{\rho Al}}\sin\frac{(2i-1)\pi\xi}{2l}(1-\cos[\omega_i(t-t_F)]), \quad t > t_F \end{cases} \tag{10}$$

The solution of the displacement:

$$u(x,t) = \sum_{i=1}^{N_i}\sqrt{\frac{2}{\rho Al}}\sin\left(\frac{(2i-1)\pi x}{2l}\right)\eta_i(t) \tag{11}$$

The solution of the internal force:

$$N_F(x,t) = EA\sum_{i=1}^{N_i}\frac{(2i-1)\pi B_i}{2l}\cos\left(\frac{(2i-1)\pi x}{2l}\right)\eta_i(t) \tag{12}$$

### 4.3. Simplified modeling of the drag-time curve

The unsteady stage of the drag-time curve was approximated by 12 sine curves. The approximation results were found to be very consistent with the original drag-time curve. However, the 12 sine loads were complex and inappropriate for engineering applications and subsequent theoretical analysis. Accordingly, it was necessary to replace the whole drag curve, denoted as $\sum_{k=1}^{12} a_k\sin(\Omega_k t+\phi_k)$ in Table 8, with fewer sine functions. The simplified modeling load would be applied on the cantilever bar. One of the most important problems was how to identify prominent sine functions in Table 8, for example, a metric was necessary to order the importance of the different sine functions. The amplitude of the sine function $a_k$ was selected as the metric in the initial investigation. The subsequent study selected $a_k\Omega_k$, which was the parameter in the amplitudes of $N_F(x,t)$, as the metric. However, poor results (shown later) were obtained using the first three sine functions ordered by metrics $a_k$ and $a_k\Omega_k$. Additional analysis was necessary to determine the metric to be used to order the importance of different frequencies compositions.

The displacement and internal force represented detailed properties of the forced vibration. A method based on the perspective of energy was attempted for the selection of the metric. The kinetic energy [26] of each vibrational model under excitation of a certain sine load could be expressed as

$$T_i = \frac{1}{2}\int_0^l \rho A\left(\frac{\partial u_i}{\partial t}\right)^2 dx = \frac{1}{\rho Al}a_k^2\Omega_k^2\sin^2\left(\frac{(2i-1)\pi\xi}{2l}\right)\frac{1}{(\Omega_k^2-\omega_i^2)^2} \times(\cos\Omega_k t-\cos\omega_i t)^2 \tag{13}$$

The potential energy [26] of each vibrational model could be expressed as

$$U_i = \frac{1}{2}\int_0^l N_F\left(\frac{\partial u_i}{\partial x}\right)dx = \frac{1}{\rho Al}a_k^2\Omega_k^2\sin^2\left(\frac{(2i-1)\pi\xi}{2l}\right)\frac{1}{(\Omega_k^2-\omega_i^2)^2} \times\left(\frac{\omega_i}{\Omega_k}\sin\Omega_k t-\sin\omega_i t\right)^2 \tag{14}$$

Thus, the amplitudes of kinetic and potential energy had the same form, given as follows:

$$A_E = \frac{1}{\rho Al}a_k^2\Omega_k^2\sin^2\left(\frac{(2i-1)\pi\xi}{2l}\right)\frac{1}{(\Omega_k^2-\omega_i^2)^2} \tag{15}$$

To represent the total energy along the whole cantilever bar, consider the end-loading condition, that is, $\xi = l$; the sum of infinite series for all modes can be expressed as

$$A_{ET} = \sum_{i=1}^{\infty}\frac{1}{\rho Al}a_k^2\Omega_k^2\frac{1}{(\Omega_k^2-\omega_i^2)^2} \tag{16}$$

Considering the integration,

$$\sum_{i=1}^{\infty} \frac{1}{[(2i-1)^2 - c]^2} = \frac{\sqrt{c}\pi^2 - \pi \sin(\sqrt{c}\pi)}{16c^{\frac{3}{2}} \cos^2(\frac{\sqrt{c}\pi}{2})} \tag{17}$$

Thus, the analytical solution of $A_{ET}$ can be expressed as:

$$A_{ET} = \frac{\rho l^3}{\pi^4 E^2} a_k^2 \Omega_k^2 \frac{\sqrt{c}\pi^2 - \pi \sin(\sqrt{c}\pi)}{c^{\frac{3}{2}} \cos^2(\frac{\sqrt{c}\pi}{2})}, \quad c = \frac{4\rho l^2}{\pi^2 E} \Omega_k^2 \tag{18}$$

Metric $A_{ET}$, noted as the energy coefficient, was the appropriate metric to order the importance of each sine compositions and it was the product of three items. The first item, $\frac{\rho l^3}{\pi^4 E^2}$, was determined by the structural parameters of the cantilever bar. The second item, $a_k^2 \Omega_k^2$, depended on the parameters of each induced sine load. The third item depends on the combined action of the sine load and natural frequencies of the cantilever bar. The energy coefficient represents the excitation energy of each of the sine loads. Specific values were assigned to the parameters of the cantilever bar to present the results based on different metrics. The first natural frequency of the beam was set as 62 Hz, and the length was 3 m; these values were close to those of the physical force measurement structure. As a result, we could reorder the sine load in Table 8, as shown in Table 9.

**Table 9**
Reordering sine loads based on the excitation energy for each sine composition.

| | $f_k$ (Hz) | $a_k$ | $\Omega_k$ | $\phi_k$ | $A_{ET}$ |
|---|---|---|---|---|---|
| $k=1$ | 77.6 | −1024.3 | 487.6 | −2.9 | 4.239E−04 |
| $k=2$ | 1676.1 | −69.1 | 10531.0 | 2.0 | 2.414E−05 |
| $k=3$ | 315.6 | −325.3 | 1983.2 | 0.1 | 2.046E−05 |
| $k=4$ | 2427.9 | −289.8 | 15255.1 | 10.6 | 1.353E−05 |
| $k=5$ | 2405.7 | −392.0 | 15115.3 | 1.7 | 2.825E−06 |
| $k=6$ | 651.9 | 334.1 | 4096.0 | 3.1 | 6.654E−07 |
| $k=7$ | 705.3 | −237.8 | 4431.6 | 1.7 | 6.448E−07 |
| $k=8$ | 166.6 | 197.7 | 1046.7 | 13.9 | 4.785E−07 |
| $k=9$ | 2344.1 | −119.6 | 14728.5 | −0.01 | 5.334E−08 |
| $k=10$ | 1626.2 | −115.0 | 10217.8 | 6.3 | 4.451E−08 |
| $k=11$ | 1518.2 | −57.8 | 9539.4 | −0.4 | 1.750E−08 |
| $k=12$ | 1022.1 | 21.1 | 6421.9 | 0.8 | 2.376E−09 |

The displacement solution $u(x,t)$ is the basic variable directly solved by eq. (5), and the internal force $N_F(x,t)$ is sensed by the balance. The results of $u(x,t)$ and $N_F(x,t)$ as a function of time

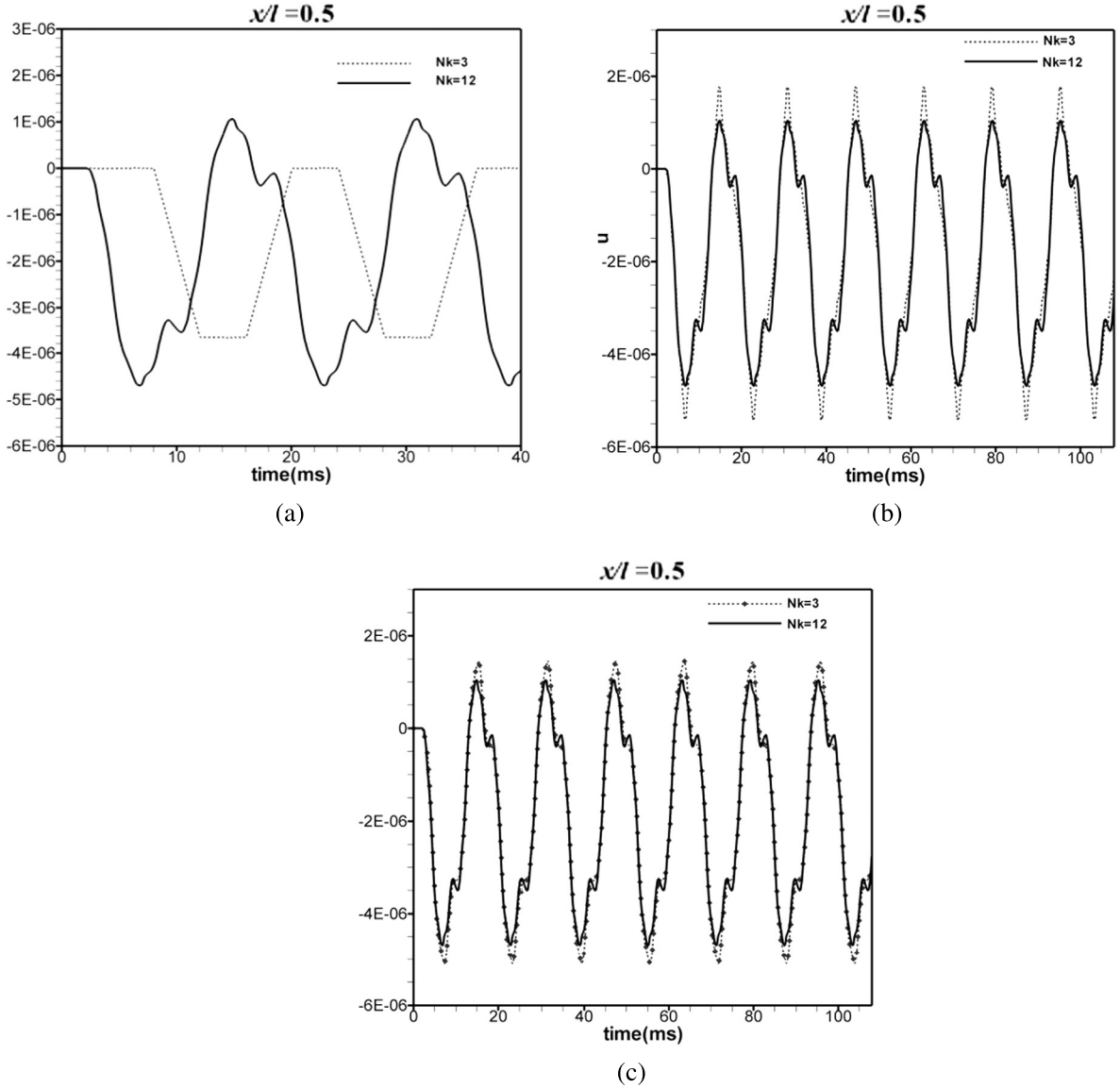


**Fig. 9.** Results of $u(x,t)$ with the first three sine loads ordered by different metrics: (a) curve corresponding to metric $a_k\Omega_k$, (b) curve corresponding to metric $a_k$, and (c) curve corresponding to the energy coefficient.

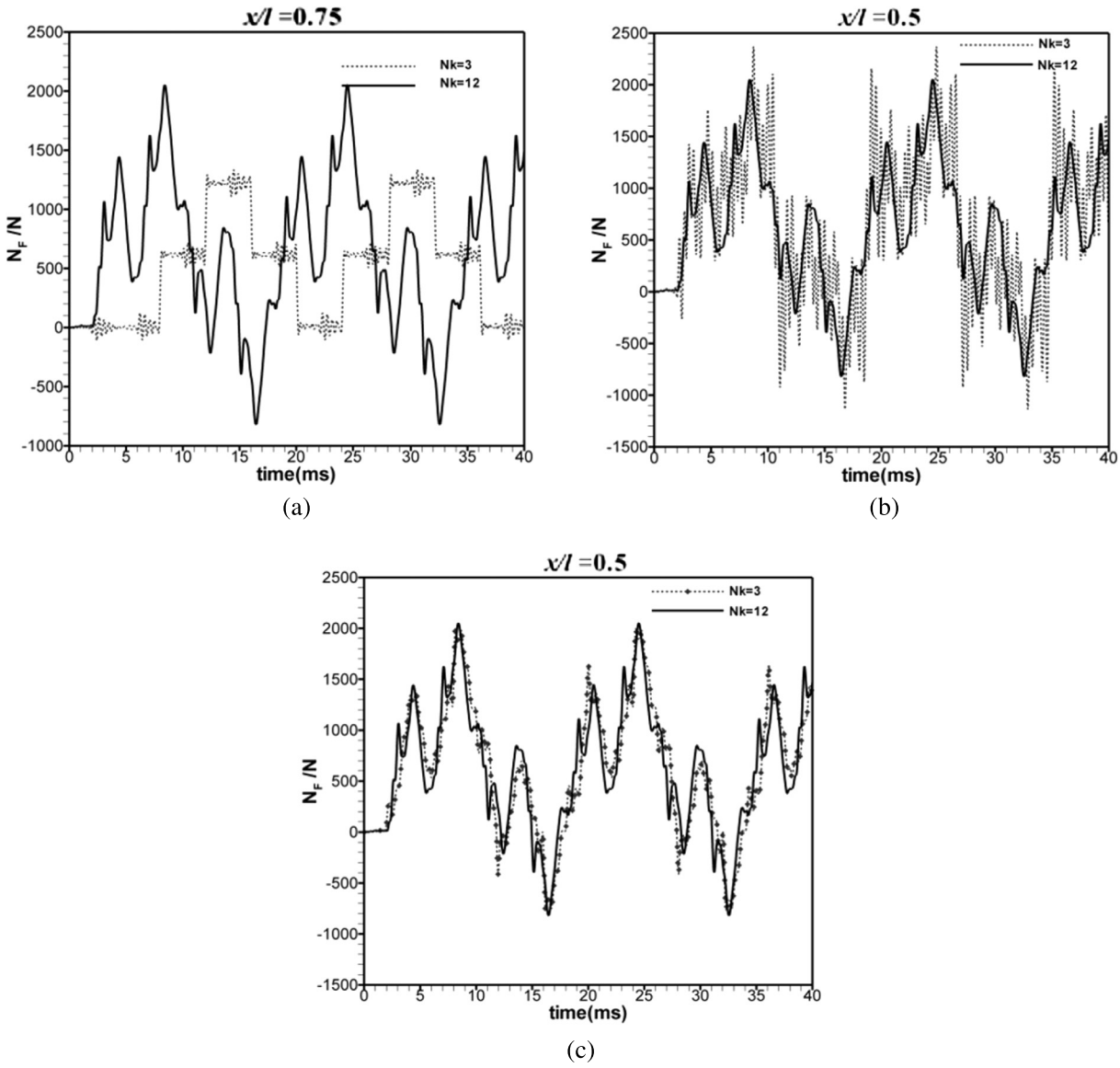


**Fig. 10.** Results of $N_F(x,t)$ with the first three sine loads ordered by different metrics: (a) curve corresponding to metric $a_k\Omega_k$, (b) curve corresponding to metric $a_k$, and (c) curve corresponding to the energy coefficient.

were of interest. Additionally, the curves of $u(x,t)$ and $N_F(x,t)$ with the excitation of the first three sine load ordered by different metrics are presented for comparison with the results of the approximated drag-time curve in Fig. 9 and Fig. 10, respectively. The balance position $x$ was selected as $x/l = 0.50$.

The results of the first three sine functions ordered by $a_k\Omega_k$ for $u(x,t)$ showed the worst effect, and the appearance of the phase and peak distortions are shown in Fig. 9(a). The results corresponding to metric $a_k$ are quite consistent with the results of the approximated drag-time curve, except for the higher value around the peaks. Moreover, the best result was obtained from the order based on the energy coefficient, which captured the appropriate phase and finer peak values. The result for $N_F(x,t)$ showed similar effects for the three metrics as illustrated in Fig. 10. The curve for metric $a_k\Omega_k$ was still the worst. The result of $N_F(x,t)$ for metric $a_k$ missed both the general shape and the peak values. The high frequency of approximately 2000 Hz in Table 8, numbered as $k = 2$ oscillations, seriously altered the degree of agreement. The best result was still obtained from the energy coefficient. Thus, the whole drag-time curve containing 12 sine functions could be replaced by the first three sine compositions in Table 9. Furthermore, an effective energy coefficient expressed in eq. (18) was derived to order the significances of different sine loads. The reason for the excellent effects for the energy coefficient was discussed. The solution $N_F(x,t)$ was closely related to the vibrational properties of the whole cantilever bar. In addition, the vibrational properties were found to be based on the combination of the actions of the drag-time curve and the natural frequencies. Metrics $a_k\Omega_k$ and $a_k$ only showed the effects of the outer excitation force. The energy coefficient contained the comprehensive information, and the properties of the drag force and structural parameters of the cantilever bar were taken into account.

## 5. Conclusion

In this paper, the characteristics of the drag-time curve of the impulse force in the axial direction and the corresponding structural vibration induced by the shock tunnel start-up process were investigated using numerical simulation and theoretical derivation, separately.

Analysis of the numerical results revealed the mechanism of the trend of the drag-time curve. There was a tight link between the

shape of the drag-time curve and the static pressure distribution along the axis of the nozzle when the PS arrived at the outlet of the nozzle. The typical wave structure was comprised of the PS, CD and SS and determined the static pressure distribution.

The features of time span and frequency composition for the drag-time curve were also investigated. The start time point of steady vibration could be estimated based on the feature of the time span. The whole start-up process encompassed an impulse stage, a transition stage and a steady stage. The unsteady time duration that included the impulse and transition stages was determined by the velocity of flow, the length scale of the wave structure and the aircraft model. A qualitative assessment was performed for the excitation degrees among the vibrational modes. The frequency composition characteristics of the impulse and transition stages were determined to be different. For the transition stage, the order of magnitude of the prominent frequencies was 100 Hz. For the impulse stage, the order of magnitude of one prominent frequency was approximately 70 Hz, and another prominent frequency was approximately 1,000 Hz, which is a much higher frequency for the force measurement structure. In addition, the forebody pressure drag was the main source of the total drag.

Theoretical modeling and simplification of the drag-time curve were also conducted, thereby making the theoretical analysis of the forced vibration possible. Furthermore, a metric noted as energy coefficient to order the significance of sine loads was derived. The drag-time curve was approximated using 12 sine curves based on the global optimization algorithm LDSE. Theoretical derivation was conducted to obtain the solutions of the displacement and the internal force. With the purpose of simplifying the 12 sine curves, the energy coefficient derived from the perspective of energy was used to reorder the significances of the 12 sine curves. The results of the internal force and displacement of the first three curves showed good agreement with the results of the 12 sine curves.

The effects of the turbulence and flow around the throat (such as curvatures of the sonic line) will be investigated in future work.

## Conflict of interest statement

The authors declare that there is not any commercial or associative interest that represents a conflict of interest in connection with the work submitted.

## Acknowledgements

This project was supported by the National Natural Science Foundation of China (grants 11472281 and 11532014) and National Key Program of Research and Development (No. 2016YFA0401200). We acknowledge Zongmin Hu, Yunpeng Wang and Chun Wang for helpful discussions.

## References

[1] Michael S. Holden, Timothy P. Wadhams, Matthew MacLean, et al., Experimental Research and Analysis in Supersonic and Hypervelocity Flows in the LENS Shock Tunnels and Expansion Tunnel, AIAA Paper, No. 2015-3660, 2015.

[2] Hideyuki Tanno, Katsuhiro Itoh, Tomoyuki Komuro, et al., Design and evaluation of strain gauge force balance with short test duration, Trans. Jpn. Soc. Aeronaut. Space Sci. 48 (2005) 1–6.

[3] Niranjan Sahoo, D.R. Mahapatra, G. Jagadeesh, et al., Design and analysis of a flat accelerometer-based force balance system for shock tunnel testing, Measurement 40 (2007) 93–106.

[4] K. Satheesh, G. Jagadeesh, Analysis of an internally mountable accelerometer balance system for use with non-isotropic models in shock tunnel, Measurement 42 (2009) 856–862.

[5] Eric C. Marineau, Force measurements in hypervelocity flows with an acceleration compensated piezoelectric balance, J. Spacecr. Rockets 48 (2011) 697–700.

[6] S. Trivedi, V. Menezes, Measurement of yaw, pitch and side-force on a lifting model in a hypersonic shock tunnel, Measurement 45 (2012) 1755–1764.

[7] G. Smolinski, Proof of Concept for Testing Acceleration Compensation Force Balance Techniques in Short Duration Flows with a CEV Capsule, AIAA Paper, No. 2007-1010, 2007.

[8] C.E. Smith, The starting time process in a hypersonic nozzle, J. Fluid Mech. 24 (1966) 625–640.

[9] T. Saito, K. Takayama, Numerical simulation of nozzle starting process, Shock Waves 9 (1999) 73–79.

[10] Anne-Sophie Mouronval, Abdellah Hadjadj, Numerical study of the starting process in a supersonic nozzle, J. Propuls. Power 21 (2005) 374–378.

[11] A-S. Mouronval, et al., Numerical investigation of transient nozzle flow, Shock Waves 12 (2003) 403–411.

[12] D. Igra, Numerical simulation of nozzle starting flow, J. Spacecr. Rockets 53 (2015) 217–224.

[13] T. Mizukaki, S. Watabe, N. Kawamura, et al., Flow Visualization of Starting Process of a Two-Dimensional Truncated Plug Nozzle Using Shock Tube, AIAA Paper, No. 2011-2315, 2011.

[14] Yunpeng Wang, Zongmin Hu, Yunfeng Liu, Zonglin Jiang, Starting process in a large-scale shock tunnel, AIAA J. 54 (2016) 1240–1249.

[15] Zonglin Jiang, Hongru Yu, Experiments and Development of Long-Test-Duration Hypersonic Detonation-Driven Shock Tunnel (LHDst), AIAA Paper, No. 2014-1012, 2014.

[16] Volkan Akcelik, Branislav Jaramaz, Omar Ghattas, Nearly orthogonal two-dimensional grid generation with aspect ratio control, J. Comput. Phys. 171 (2001) 805–821.

[17] Klaus A. Hoffmann, Steve T. Chiang, Computational Fluid Dynamics, Engineering Education System, Wichita, Kansas, 2000, p. 69.

[18] Hanxin Zhang, NND schemes and numerical simulation of axial symmetric free jet flows, Acta Mech. Sin. 6 (1990) 193–203.

[19] Yunfeng Liu, Yunpeng Wang, Chaokai Yuan, Changtong Luo, Zonglin Jiang, Aerodynamic force and moment measurement of 10° half-angle cone in JF12 shock tunnel, Chin. J. Aeronaut. 20 (2017) 983–987.

[20] Hewu Chen, Investigation on the link-up between the aerodynamic force data measured in supersonic and hypersonic wind tunnel, Acta Aerodyn. Sin. 9 (2000) 345–349 (in Chinese).

[21] Yaodong Yang, Fu Wang, Dahua Guo, Aerodynamic measurements of 10° half-angle cone in hypersonic impulse tunnel with six-component balance, J. Exper. Fluid Mech. 1 (1988) 60–63 (in Chinese).

[22] George S. Pick, Base pressure distribution of a 10° sharp cone at hypersonic speeds and high angles of attack, in: AIAA 7th Thermophysics Conference, San Antonio, April 10–12, 1972, AIAA 72-316, pp. 2–11.

[23] C.T. Luo, B. Yu, Low dimensional simplex evolution: a new heuristic for global optimization, J. Glob. Optim. 52 (2012) 45–55.

[24] C.T. Luo, C. Wang, Z.L. Jiang, S.-L. Zhang, A metamodel-assisted evolutionary algorithm for expensive optimization, J. Comput. Appl. Math. 236 (2011) 759–764.

[25] Baoqing Meng, Guilai Han, Zonglin Jiang, Theoretical investigation on aerodynamic force measurement interfered by structural vibrations in large shock tunnel, Chin. J. Theor. Appl. Mech. 48 (2016) 102–110 (in Chinese).

[26] Zhenhua Ni, Vibration Mechanic, Xi'an JiaoTong University Press, Xi'an, 1989.